FLSEVIER

Contents lists available at ScienceDirect

# Materials and Design

journal homepage: www.elsevier.com/locate/matdes



# Effect of ultrasonic energy on the spot weldability of aluminum alloy AA6061



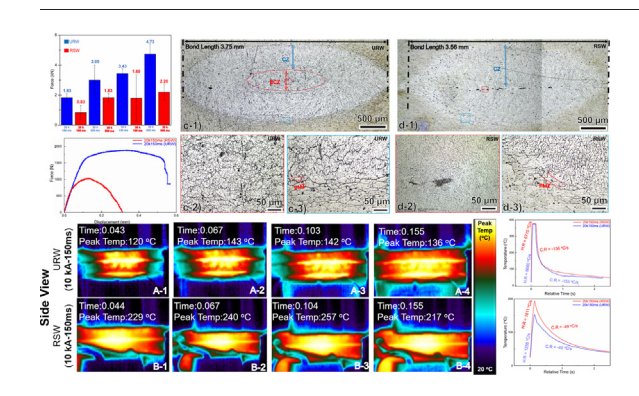
Umair Shah. Xun Liu\*

The Ohio State University, EJTC, 1248 Arthur Adams Drive, Columbus, OH 43221, United States of America

#### HIGHLIGHTS

- Ultrasonically assisted resistance spot welding (URW) improves the mechanical properties of the welds of aluminum alloy.
- Ultrasonic energy promotes formation of equiaxed crystal zone in the weld nugget.
- Ultrasonic energy assists in the removal of RSW weld defects.
- Infrared thermography reveals lower temperature during URW than RSW.

#### GRAPHICAL ABSTRACT



#### ARTICLE INFO

Article history: Received 15 January 2020 Received in revised form 24 March 2020 Accepted 26 March 2020 Available online 29 March 2020

Keywords: Resistance spot welding Power ultrasonics Aluminum joining Contact resistance Infrared imaging

#### ABSTRACT

This study investigates the effects of superimposed ultrasonic vibration on resistance spot welding (RSW) of aluminum alloy AA6061-T6. A novel ultrasonically assisted resistance spot welding process, referred to as ultrasonic resistance welding (URW), is applied to weld AA6061 at various conditions and compared with the results from RSW. Lap shear tensile tests of URW welds show significantly improved mechanical properties, including higher strength, better ductility and higher amount of energy absorbed prior to failure compared with RSW welds. Optical micrographs of the weld cross section show that the ultrasonic vibration enhances nugget formation and minimizes porosities defects. Besides, equiaxed crystal structure is generally observed in the nugget center of URW welds whereas the majority of RSW fusion zone is dominated with columnar grain structure. In situ thermal imaging of the two processes shows a lower temperature distribution, smaller heating and cooling rates during URW. This is attributed to the ultrasonically assisted fracture and breakdown of surface oxides and contaminates, which reduces the contact resistance and accordingly heat generation rate.

© 2020 The Authors. Published by Elsevier Ltd. This is an open access article under the CC BY-NC-ND license (http://creativecommons.org/licenses/by-nc-nd/4.0/).

# 1. Introduction

Resistance spot welding (RSW) is one of the most widely used joining processes in automotive and aerospace industry based on its numerous advantages, such as ease of automation, self-clamping, high

\* Corresponding author. E-mail address: liu.7054@osu.edu (X. Liu). reliability, and high production rate [1]. During RSW, a high amount of electrical current is passed through a pressurized zone for a short duration of time, followed by rapid melting, nugget formation and solidification. There are typically around 5000 spot welds in an automobile body [2]. Integrity on mechanical properties of these joints is critical for the safety of passengers in case of vehicle crash.

Nowadays, growing concerns of energy consumption and global warming increases the demand for lightweight vehicles. As one of the

promising materials with high specific strength, aluminum alloys have received increasing attention in the automotive industry these years, for example, the entire body of Ford 150 truck is manufactured from aluminum [1,3]. On the other hand, RSW for aluminum alloys is relatively challenging despite its widespread and robust applications on joining steel. This on one hand is because the electrical and thermal conductivities of aluminum alloy are much higher compared with steel. Accordingly, a higher welding current is generally required. Moreover, the stable oxide layer on the surface of aluminum alloys creates higher contact resistance and instability during the process, which reduces repeatability of weld quality and leads to rapid electrode wear [1,4]. To facilitate RSW of aluminum alloys, this oxide layer needs to be effectively removed. Conventional methods include sample surface preparation through mechanical grinding or chemical cleaning with certain reagents, for example, NaOH. Increasing electrode force during RSW also helps with the squeezing and breakdown of the oxide layer. James et al. reported that a small relative rotation (1°) under 1 kN force on coated aluminum can significantly reduce the contact resistance from 7000  $\mu\Omega$  to 110  $\mu\Omega$  [5]. Pre-pulsing is another method to modify the contact resistance and improve RSW process robustness for aluminum [6-9]. Luo et al. applied a pre-pulse of 8 kA with 50 ms under 3 kN force for AA5052 spot welds and reported the weld strength increased from 1.4 kN to 2.1 kN [9]. Similarly, Han studied AA5754 and AA6111 and found that pre-pulsing is able to suppress expulsion and improve process robustness [7].

The rapid melting and solidification during RSW could generate high residual stress and solidification defects, such as cracks and porosities. Compared with steel, aluminum is more prone to such discontinuities due to its higher thermal expansion coefficient and wider solidification range [10]. Besides, molten aluminum has higher affinity with hydrogen and can absorb up to 0.8 cm<sup>3</sup>/100 g, which facilitates cold cracking [11]. Generally, to minimize aluminum solidification defects, there are two categories of solutions from mechanical and chemical perspectives. In the mechanical approach, Abramov et al. [12] employed hydrodynamic stirring and ultrasonic treatment during casting of various aluminum alloys. In their studies, the ultrasonic irradiated samples showed higher ductility with improved microstructure, including refined grains, suppressed columnar dendrites, increased homogeneity and reduced element segregation. Eskin et al. [11] attributed these microstructure modifications to the cavitation and acoustic streaming effects associated with the ultrasonic vibration. They were also able to directly observe bubbles through in situ synchrotron radiation imaging. In the presence of ultrasonic energy, cavitation bubbles act as small pumps that remove dissolved hydrogen from the melt [13]. Regarding chemical solutions, Knuutinen [14] reported fibrous eutectic silicon with the additions of Ba and Ca and refined plate-like eutectic silicon with the additions of Y and Yb in cast A356 aluminum alloy. Similarly, Shivkumar [15] summarized the effect of Ti-B, Sr and Na on different groups of cast aluminum alloys and reported significant improvements of microstructure with these modifiers. Comparing the mechanical and chemical solutions to remove solidification defects, the main advantage of mechanical method is its universal applicability to all alloys whereas chemical additions closely depend on the composition of specific alloy system [16].

In this study, effects of ultrasonic vibrations on RSW of aluminum alloy AA6061 are investigated. The various nonlinear physical phenomena induced by ultrasonic energy are considered to improve spot weldability of aluminum alloys in multiple aspects. In our previous study on ultrasonically assisted resistance spot welding (URW) of aluminum to steel, high speed video shows that ultrasonic vibrations help to remove the oxide layer and other surface contaminants [17]. This modifies the electrical contact resistance in the beginning stage of RSW and accordingly the weld nugget formation. Moreover, the Peltier effect at the electrode-sheet interface could be attenuated, which increases the overall electrode life [18]. In the molten aluminum, acoustic streaming and cavitation effects can alter material flow. At the liquid-solid interface, ultrasonic energy induces micro-jetting, shock stress

and radiation pressure, which could facilitate heterogenous nucleation and enhance production of refined microstructure.

On the other hand, ultrasonic spot welding (USW) is a solid state joining process that utilizes frictional heating due to high frequency shear vibrations at the faying surfaces, followed by dispersion of the undesirable contaminants and oxide layer, and a solid state joint is attained [19,20]. Mohammed et al. investigated the USW of AA 5182 alloy and reported the peak load of 6 kN and failure energy of 8 I during tensile tests of the weld, which satisfies the AWS D17.2 standard [21]. Although USW shows to be an efficient joining process, its applications are mainly restricted to thin gage sheets and softer materials due to the limited power of generally available ultrasonic transducers. For improvement, Yang and Cao [22] developed an electrically assisted ultrasonic spot welding process, during which electrical current was applied prior to ultrasonic welding. Their hybrid method resulted in an 80% increase in the mechanical strength of conventional ultrasonic welds of Cu and Al, Different from their approach, Shah and Liu [23] developed an ultrasonic resistance welding (URW) process, during which ultrasonic vibrations are superimposed on resistance spot welding (RSW). The experimental system is based on a regular RSW welding machine where the bottom electrode is connected to an ultrasonic transducer and serves as a sonotrode simultaneously. Comparing with RSW welds at the same electrical current condition, URW welds have shown great improvement of mechanical properties in both aluminum to steel [24] and steel to steel [23] joints.

In this study, URW of aluminum alloy AA6061 were systematically studied and compared with RSW at different conditions. In situ thermal imaging is performed to reveal the ultrasonic effects on the temperature field evolution during the welding process. Mechanical properties and microstructure of the welds were evaluated.

#### 2. Experimental details

#### 2.1. Materials

Commercially available AA6061 sheets (Si: 0.561, Mg: 0.986, Cu: 0.310, Fe: 0.289, Mn: 0.052, Zn: 0.024, O: 0.018, from McMaster) with dimensions of  $70^Lx25^Wx1.6^T$  mm<sup>3</sup> are used in this study. The AA6061 sheets are cold rolled with the T6 tempered condition, the specifications of which met ASTM B209 and AMS 4027 standards. T6 tempering is a two-stage process i.e. quenching at 500 °C, followed by aging at 180 °C. Fig. 1 shows the microstructure of the as-received AA 6061 alloy (etched with Keller's reagent). The black dots correspond to dispersed second phase particles, which is frequently observed in the deformed and heat treated wrought aluminum alloys [25,26].

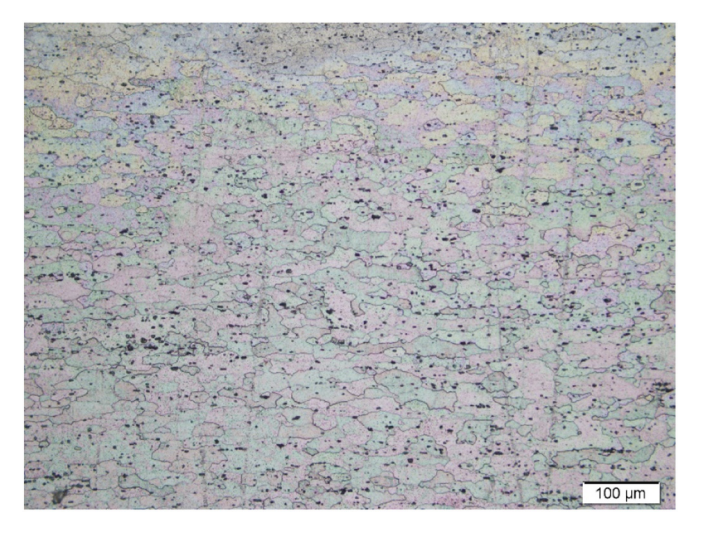


Fig. 1. Optical micrograph of the grain structure in the as received Al-6061 alloy.

**Table 1** Energy comparison for RSW and URW process.

	RSW				URW			
Welding current (A)	20,000		30,000		20,000		30,000	
Welding time (s)	0.15	0.5	0.15	0.5	0.15	0.5	0.15	0.5
Secondary voltage (v)	8.25	8.25	8.30	8.31	8.27	8.26	8.33	8.35
Ultrasonic power (Watts)	0	0	0	0	700	700	700	700
RSW energy (J)	24,750	82,500	37,350	124,650	24,810	82,600	37,485	125,250
Ultrasonic energy (J)	0	0	0	0	105	350	105	350
Total energy (J)	24,750	82,500	37,350	124,650	24,915	82,950	37,590	125,600

# 2.2. URW setup

The URW system is developed based on an RSW machine and detailed descriptions are provided in our previous works [17]. The tip diameter of top and bottom electrode is 12 mm. The electrical current is measured via a Rogowski coil and a self-developed LabView program digitally controls the start-and-off time of the ultrasonic vibration. The ultrasonic vibration is triggered based on the AC electrical current and continues for the same amount of time as the current. The ultrasonic vibration amplitude in the unloaded condition is 34 µm (peak to peak). Other process parameters include AC current (60 Hz) with root mean square magnitude of 20 kA, 30 kA and durations of 150 ms, 500 ms. The applied welding force is around 2.67 kN. URW and conventional RSW are performed at the same electrical current conditions for benchmarking and comparison. The electrical energy for RSW and ultrasonic energy for URW process are estimated via Eqs. (1) and (2) respectively. Energy inputs into the two processes are summarized in Table 1. It can be observed that overall in the URW process, the ultrasonic energy contributes to less than 2% of RSW energy.

$$E_{RSW}(J) = Secondary\ Voltage\ (Volts) \times Welding\ current\ (Amps) \times Welding\ Time\ (s)$$
 (1)

$$E_{UA}(J) = Power(Watts) \times Welding Time(s)$$
 (2)

# 2.3. Thermal imaging of the URW process

Evolution of the temperature distribution during the welding process was captured through a non-contact infrared (IR) camera at a frame rate of 30 Hz. Each frame consists  $640 \times 480$  discrete intensity measurements. The IR camera was mounted in two different positions relative to the sheets, i.e. top and side configuration as shown in Fig. 2. In the side view, the two sheets are placed at the center half of the electrodes, revealing the edge surface as a pseudo-weld cross section. Since the effective contact area is reduced in half, lower electrical current is selected for the same level of current density as the actual welding process and avoid large expulsion. In this view, 10 kA with 150 ms and 500 ms, as well as 20 kA with 150 ms welding conditions were studied. At 10 kA, 500 ms and 20 kA, 150 ms a little melting and ejection of molten metal was recorded. In the top view, since the welding configuration essentially remains unchanged as the actual URW process, the same welding parameters are selected to capture instantaneous images of the spot weld. To protect the IR camera from potential expulsion of

# Real Time Temperature Measurement

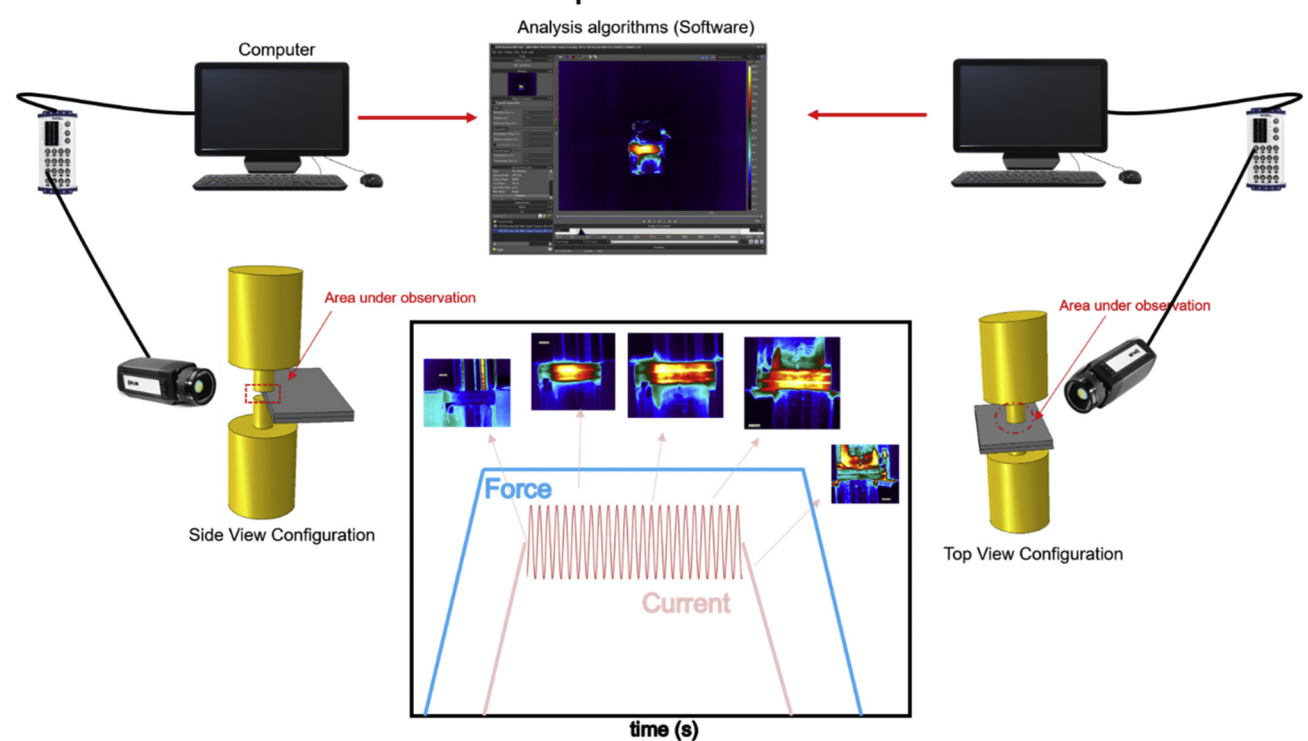


Fig. 2. Side and top configuration for thermal imaging.

molten aluminum, a Germanium anti reflection coated filter with a range of 3 to 12  $\mu m$  and transmittance greater than 95% was installed in front of the camera lens. The operating range of the camera with the selected calibrated lens filter is from 10 °C to 375 °C. Regions above this maximum temperature limit of 375 °C are represented with sharp red color in the infrared images.

#### 2.4. Weld characterization

Lap shear tensile tests of the welds were performed via a MTS 800 test machine at a rate of 1 mm/min. The tensile direction is parallel to the sheet rolling direction. Detailed geometries are provided in Fig. 3. Restraining shims are placed at the two ends to ensure co-planar loading. Hardness measurements on the welds are performed with a load of 100 g for a duration of 15 s, and 150  $\mu$ m spacings between indentations. Microstructure of the weld is characterized by light optical (OLYMPUS GX71) and scanning electron microscope (FEI Apreo LoVac). Metallurgical samples are sectioned along the weld center, ground and polished following standard preparation procedures. The samples are finally etched with Keller's reagent (95 mL H<sub>2</sub>O, 2.5 mL HNO<sub>3</sub>, 1.5 mL HCl & 1.0 mL HF) to reveal the grain structure.

#### 3. Results and discussion

#### 3.1. Mechanical properties comparisons

Fig. 4(a) compared the peak load during lap shear tensile tests of RSW and URW welds and the area under the load-displacement curve, representing the energy absorbed prior to failure. In all the tested conditions, URW welds show a significantly higher strength than conventional RSW welds. At 20 kA and 150 ms, URW welds are fractured at an average load of around 1.83 kN compare to 0.83 kN in the absence of ultrasonic energy. The highest weld strength was obtained at 30 kA and 500 ms, where the average peak load for URW is around 4.73 kN while only 2.20 kN for RSW samples. Energy absorption is considered to be a more accurate indication of the load carrying capacity for spot welds [27]. For all the investigated welding conditions, URW joint absorbed energy more than twice as that of RSW joints. These improved mechanical behaviors are directly reflected by the load displacement curves of the welds during tensile tests, and the typical ones at different electrical and ultrasonic parameters are provided in Fig. 4(b-e). Furthermore, a higher stiffness (shown as the S value on the curve) is observed in URW welds with more resistance to deformation, which could be a result of larger nugget and refined microstructure.

At 30 kA and 500 ms condition, URW specimen exhibited partial interfacial failure mode. In remaining scenarios, interfacial failure mode is observed. Fracture of the spot weld is a competition between crack propagation through the weld nugget known as interfacial debonding and twisting around the weld nugget known as nugget pullout. In interfacial failure mode, shear stress dominates between sheets while in the nugget pullout failure mode, tensile stress dominates in the weld zone [28]. Fig. 3 schematically illustrates the stress distribution pattern during the interfacial (path A) and nugget pullout failure mode (path C). In path C, necking occurs at the tensile region adjacent to nugget

(legs) on the top and bottom sheets unevenly, followed by localized stress concentration and fracture of the weld [29]. Local variations of microstructure and properties could result in mixed partial interfacial failure mode (path B). In this scenario, as the crack propagates and encounters a macroscopic strengthening site, it will detour its path and propagate through the nearby soft region. A larger weld nugget is more restraining and generally requires a higher force for shearing or twisting, which accordingly increases the maximum failure load. On the other hand, this strengthening effect can be directly deteriorated if weld defects, for example, porosities are present.

Fig. 5 compares the microhardness distributions on RSW and URW welds at various conditions. Overall, lower hardness is observed in the weld nugget compared with the base metal, which can be attributed to the dissolution of strengthening precipitates [1]. In between the nugget and the base material, a narrow transition region exists, which corresponds to the heat affected zone and the decrease of hardness is related to coarsening of precipitates. At 20 kA 500 ms, URW and RSW welds have shown similar hardness values in the nugget center even though in the microstructural perspective, URW contains equiaxed crystals while RSW contains columnar grains in this location. In the adjacent region surrounding the center, URW welds show slightly higher hardness that RSW welds. This indicates the formation of the equiaxed crystal zone will modify the element distribution in the columnar zone, which accordingly change the hardness distribution. In the first three weld conditions, i.e. 20 kA 150 ms, 20 kA 500 ms and 30 kA 150 ms, the low hardness in the weld nugget leads to interfacial debonding. On the other hand, in the case of 30 kA 500 ms, URW weld shows slightly higher hardness at the weld nugget than the RSW weld and welds at other conditions. This contributes to the partial interfacial failure mode observed during lap shear tensile tests.

#### 3.2. Weld microstructure comparison

Microstructure of the weld is a function of base metal composition and the thermo-mechanical history during the welding process. The solidification behavior is governed by the heat extraction rate at the solidliquid boundary and accordingly determines formation if different types of microstructure [30,31]. The weld cross section can overall be divided into three main regions, i.e. fusion zone (FZ), heat affected zone (HAZ) and base metal. HAZ is further composed of the precipitated and recrystallized zones. Outside of the recrystallized zone is the base metal. At the boundary between FZ and HAZ, there is a narrow band of partially melted zone (PMZ). In the fusion zone of the welds obtained from this study, two types of microstructures were generally observed, as shown in Fig. 6. Type A contains an equiaxed grain structure in the center, surrounded by columnar grains. The equiaxed grains can be a single  $\alpha$ -Al phase or a bimodal structure with  $\alpha$ -Al and second phase particles. On the other hand, type B only contains columnar grains. These different forms of microstructure are obtained at different welding conditions.

Fig. 7(a) and (b) compares URW and RSW welds obtained at the electrical current condition of 20 kA with 150 ms duration. Bond length of URW weld is around 3.2 mm whereas for RSW weld is 4.6 mm. In other words, at the condition of low magnitude and short duration of electrical current, RSW has a larger nugget size than URW. However,

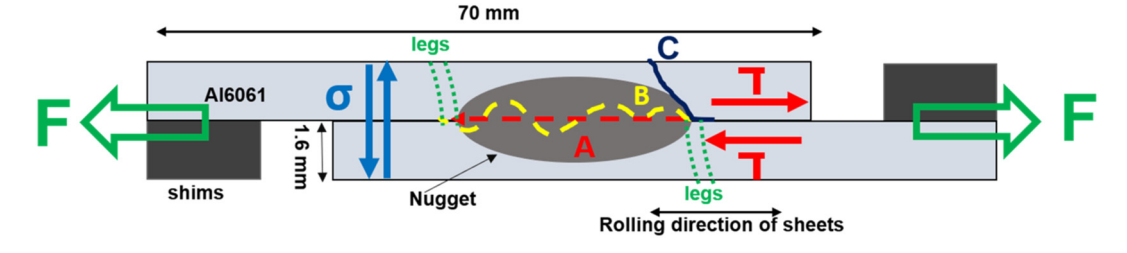


Fig. 3. Simple model showing various paths for crack propagation i.e. A (interfacial failure), B (Partial interfacial failure) & C (Nugget pull out failure) and stress distribution at interface and around nugget during load displacement test.

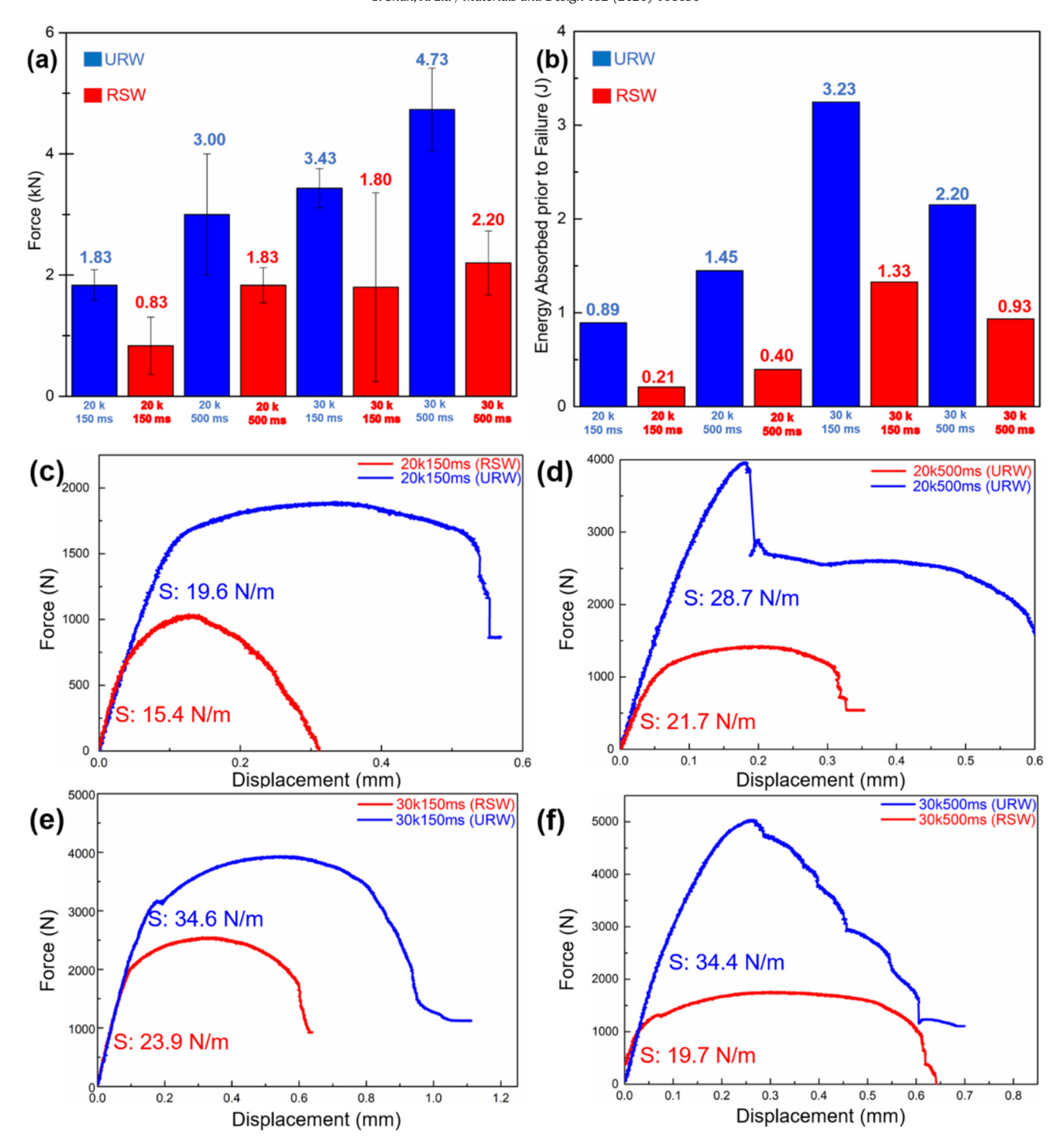


Fig. 4. (a) Maximum load measured during lap shear tensile test. (b) Area under the load displacement curve prior to failure. (c-f) load displacement curves for RSW and URW at various conditions. Here S corresponds to the slope or stiffness.

large scale voids were observed in the center of the RSW weld, as shown in the Fig. 7(b-1), which directly leads to a low average strength of 0.83 kN with a large variance for these RSW welds. These porosities are likely to be generated from aluminum shrinkage at the end of solidification. As a comparison, in the center of the URW weld fusion zone, a bimodal equiaxed crystal structure (ECZ) is observed, as shown in Fig. 7(a-2). These equiaxed grain structure helps to preserve the weld strength even though the nugget size is relatively small. Lou et al. [30] observed similar microstructure and identified the whitish region in the microstructure (Fig. 7a-2) to be  $\alpha$ -Al and the other region to be  $\beta$ -Al\_3Mg\_2 secondary precipitates. Fig. 7(a-3) shows the partially melted zone (PMZ) and heat affected zone (HAZ).

Fig. 7(c) and (d) compares URW and RSW welds obtained at 20KA with a longer duration of 500 ms current. Similar to the 150 ms current condition, the URW fusion zone contains an equiaxed crystal zone (ECZ) surrounded by the columnar grains (Fig. 7c-1) while that of the RSW weld is primarily columnar structure. Certain amount of porosities can still be observed in the center of the RSW weld but the size is greatly reduced. These porosities are detrimental to RSW weld whereas the equiaxed structure enhances the URW weld properties. Accordingly, a higher strength is observed on the URW weld. It is also noticed that for RSW welds at 20 kA, large variations in optical micrographs were observed, including the size and shape of the nugget and appearance of the porosities. These variations could be due to the instabilities during RSW

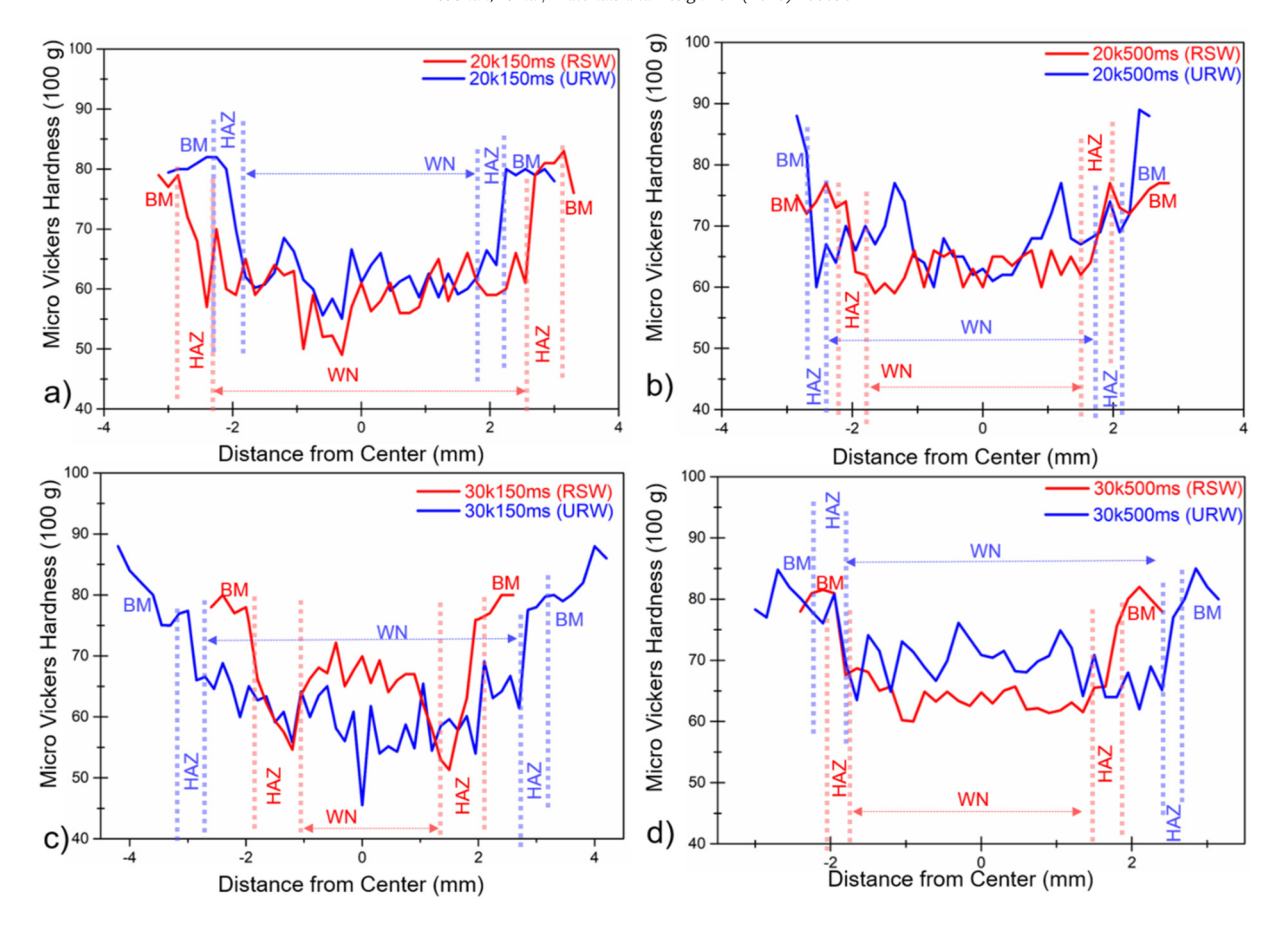


Fig. 5. Microhardness profile for RSW and URW spot welds. WN: Weld nugget; BM: Base metal; HAZ: Heat affected zone.

at low current condition to form nugget, which is also reflected in the variations of weld strength.

By increasing the electrical current length from 150 ms to 500 ms, the ECZ zone of URW weld is dominated by the whitish area of the  $\alpha$ -Al phase and the bimodal structure disappeared.

Fig. 8 compares the URW and RSW welds at higher magnitude current condition of 30 kA. With a higher current, the bond length of

URW welds greatly increases (Fig. 8a-1, c-1). In RSW welds, the porosities are effectively removed (Fig. 8b-1, d-1). At both 150 ms and 500 ms current durations, the nugget size of URW is significantly larger than that of the RSW joint. Similar to the URW weld at lower current condition, its fusion zone contains the ECZ structure in the weld center, surrounded by the columnar grains. With short duration of current, the ECZ zone comprises of bimodal structure of  $\alpha\text{-Al}$  and second phase  $\beta\text{-}$ 

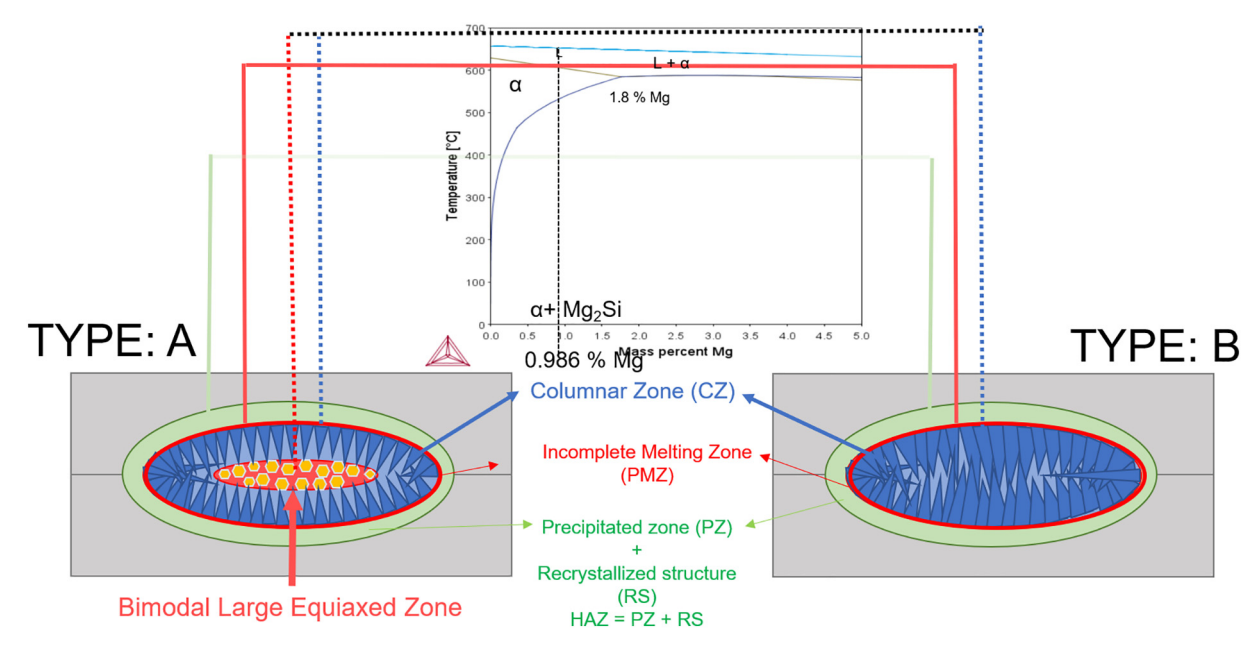


Fig. 6. Illustration of weld microstructure obtained from different process conditions. (The phase diagram is calculated from Thermo-Calc® software).

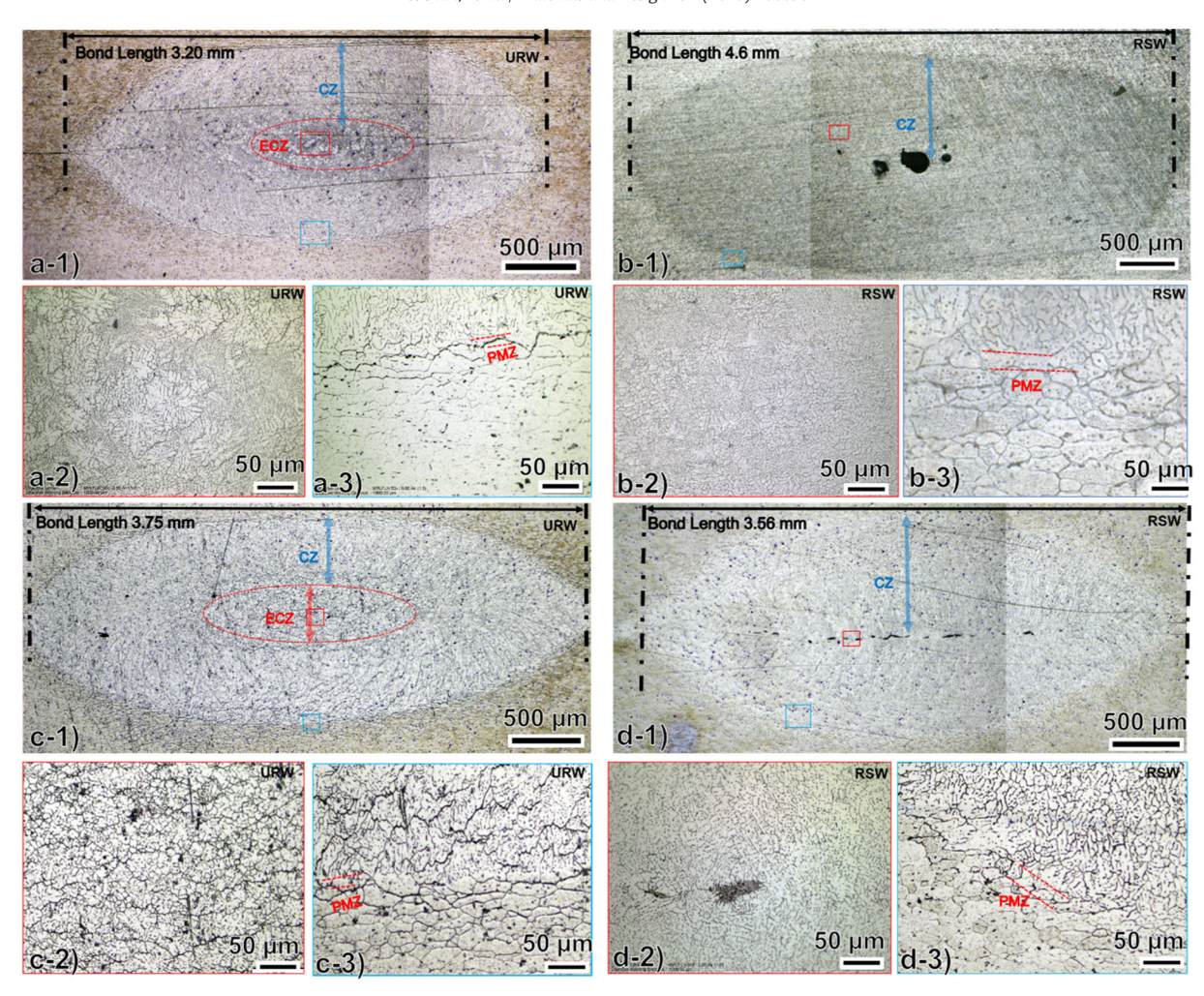


Fig. 7. Optical micrographs showing the weld microstructure for (a) RSW at 20 kA 150 ms, (b) URW at 20 k 150 ms, (c) RSW at 20 k 500 ms, (d) URW at 20 k 500 ms. ECZ: equiaxed crystal zone, CZ: columnar zone, PMZ: partial melted zone.

particles (Fig. 8a-2), which could be Mg<sub>2</sub>Si, AlSi, AlSiMg, or other metastable phases. By increasing the current length to 500 ms, this bi-modal structure is removed and the ECZ is homogenized without formation of large second phase particles. Regarding RSW welds, the fusion zone is mainly composed of columnar grains with 150 ms length of current. At a longer current duration of 500 ms, ECZ starts to form in RSW welds.

Table 2 summarizes the microstructure features of URW and RSW joints at various conditions. Overall a larger weld nugget corresponds to a higher peak load during weld lap shear tensile tests. All URW welds show an ECZ structure in the center of the weld nugget whereas the majority of RSW joints only contains columnar zone, also known as cellular dendritic zone, in the nugget except at the condition of 30 kA, 500 ms. ECZ in URW welds at 20 kA 150 ms and 30 kA 150 ms consists of bimodal structure with  $\alpha$ -Al and second  $\beta$ -phase particles. The longer duration of electrical current resulted in a more homogenized element distribution and significantly reduced the second  $\beta$ -phase particles in ECZ. At 20 kA (150 ms & 500 ms), RSW welds showed an inferior tensile strength due to the porosities in the microstructure.

Regarding the ECZ generally observed in the URW welds, Li et al. [32] were able to achieve a similar microstructure by placing two permanent magnets between top and bottom electrode during RSW process. The electromagnetic stirring effect promoted formation of ECZ by breaking down the primary dendrites during the solidification process. This indicates the superimposed ultrasonic vibration has a similar stirring effect on the melted aluminum pool during RSW. Higher magnified SEM images of the weld nugget center at different conditions are provided in Fig. 9. Combinations of different detector segments were used to reveal

individual features at the surface. For 30 and 20 kA, 150 ms URW welds, the center contains equiaxed bimodal structure with  $\alpha\text{-Al}$  and  $\alpha\text{-Al}+$  secondary  $\beta$  phase. The second  $\beta$  phase exists in the shape of round dots (Fig. 9a). As a comparison, for RSW 20 kA 500 ms where only columnar structure is formed, these  $\beta$  phase particles exist in the needle morphology in the columnar zone and are assembled in a pattern like daffodil flowers (Fig. 9c). EDS chemistry analysis shows presence of Al and Si in these flowers. In RSW welds at high current and long duration (30 kA, 500 ms), round  $\beta$  particles can be observed in the columnar zone, are shown in Fig. 9b.

# 3.3. Infrared thermography

Side view of the temperature distribution on the workpiece sheets and electrodes is provided in Fig. 10. From left to right, the thermal graphs show evolution of temperature distribution in the beginning, middle and end stage of the welding process. Fig. 10(A) represents the URW process at 10 kA, 150 ms. At 0.067 s, the peak temperature measured in URW was 143 °C (Fig. 10A-2), whereas it was 240 °C in RSW (Fig. 10B-2). The lower peak temperature could be attributed to the superimposed ultrasonic vibrations, which generate relative movements between the sheets. This facilitates breakdown of surface oxide layer and removal of contaminants. Accordingly, the overall contact resistance is reduced, and the peak temperature is lower with a smaller heat generation rate. Similar trend between URW and RSW process was also observed at 10 kA 500 ms (Fig. 10C, D). The peak temperature occurs at around 0.437 s for the two processes, which in RSW is 288 °C

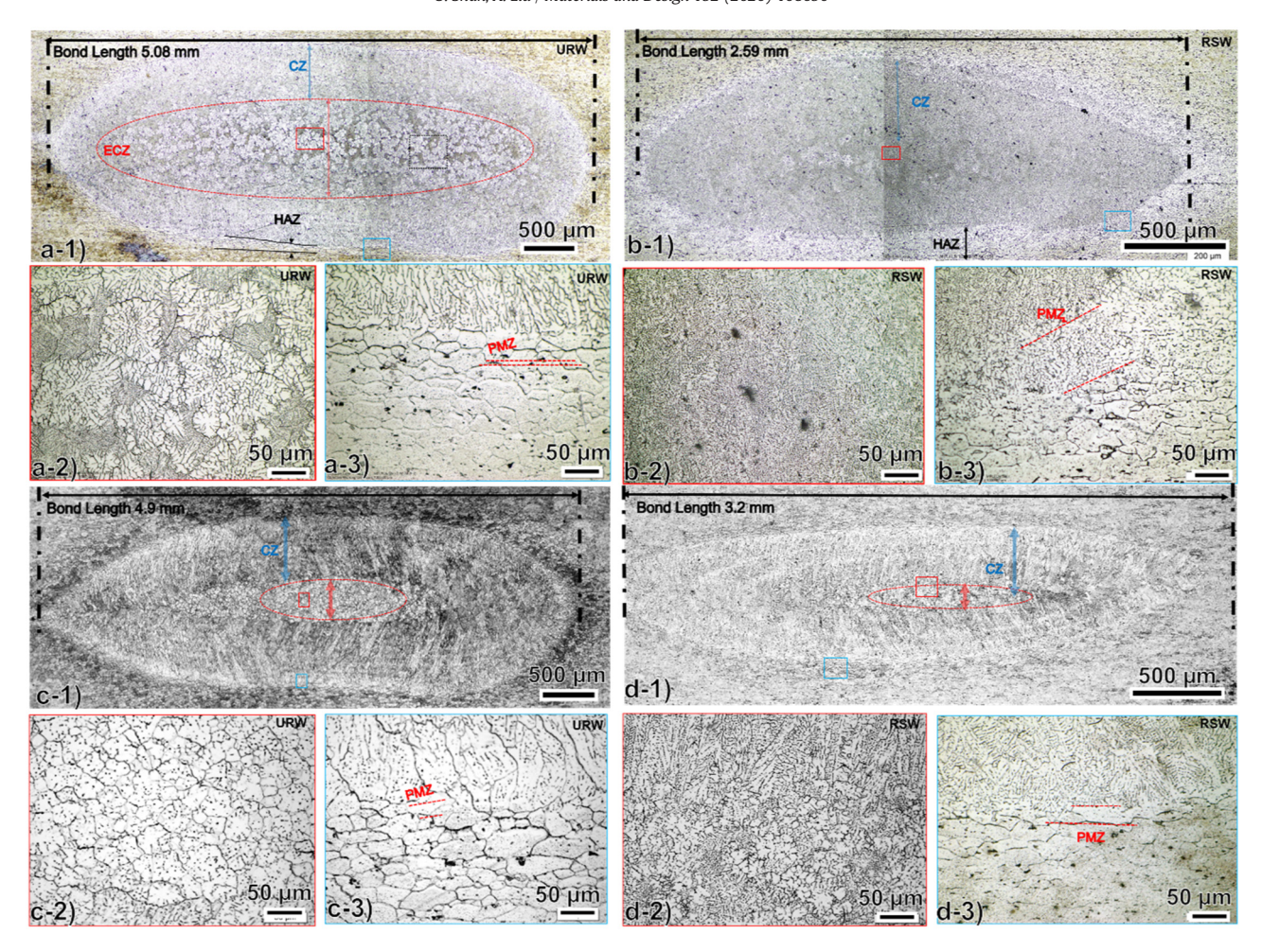


Fig. 8. Optical micrographs showing the weld microstructure for (a) RSW at 30 kA 150 ms, (b) URW at 30 k 150 ms, (c) RSW 30 k 500 ms, (d) URW 30 k 500 ms. ECZ: bimodal equiaxed zone; CZ: columnar zone; PMZ: partial melted zone.

whereas URW is 136 °C. At 20 kA 500 ms, RSW process starts to show peak temperature greater than 375 °C after 0.029 s whereas this peak temperature is not observed in URW process until after 0.106 s. Comparing with the short current duration of 150 ms, the dwell time at high temperature is longer with 500 ms. Fig. 10(E) and (F) compares the URW and RSW temperature results in the case of 20kA and 150 ms. The pink area in the center of the weld represents the thermally overexposed region due to the limit of the camera filter, which is 375 °C. It can be observed that RSW process has a larger high temperature area above 375 °C in the weld center, indicating the temperature field is higher in RSW compared with URW process.

Fig. 11 shows the extracted temperature history from the thermal graphs in Fig. 10 at different process parameters. In the side view, this thermal history corresponds to the maximum temperature at the interface region between the two sheets during the process. At 10 kA

condition (Fig. 11a, b), the temperature increases at a faster rate and reaches to a higher maximum value for the RSW process compared with URW. For a more quantitative comparison, the heating rate (H.R.) can be estimated by the slope in the most linear region (0 ms-50 ms) from the start of the weld and the cooling rate (C.R.) can be estimated by the slope of the thermal profile after the peak temperature with the period of 50 ms. At 10 kA 150 ms, RSW process shows a higher heating rates of 4076 °C/s compared with URW process of 2054 °C/s. After the peak temperature, a higher cooling rate is also observed for RSW than URW, possibly due to larger thermal gradient. This trend is similar for a longer duration of electrical current with 500 ms, as shown in Fig. 11b. A longer thermal cycle is generally observed for both RSW and URW process compared with the 150 ms case. In the third condition of higher current magnitude of 30 kA and long duration of 500 ms (Fig. 11c), the heating rate of RSW is slightly higher than

**Table 2**Values calculated form optical images showing comparison between URW and RSW joints at various conditions.

	Ultrasonic resistance welding				Resistance spot welding			
	20kA 150 ms	20kA 500 ms	30kA 150 ms	30kA 500 ms	20kA 150 ms	20kA 500 ms	30kA 150 ms	30kA 500 ms
BL (mm)	3.2	3.75	5.08	4.9	4.6	3.56	2.59	3.2
FZ	ECZ+CZ	ECZ+CZ	ECZ+CZ	ECZ+CZ	CZ	CZ	CZ	ECZ+CZ
ECZ (µm)	510 (BM)	441	429 (BM)	298	0	0	0	267
CZ (µm)	530	411	236	421	1006	672	445	232
PMZ	Narrow	Narrow	Narrow	Narrow	Wide	Wide	Wide	Narrow
HAZ	Narrow	Narrow	Narrow	Narrow	Wide	Wide	Wide	Wide

(BL: bond length, FZ: fusion zone, ECZ: equiaxed crystal zone, CZ: columnar zone, PMZ: partially melted zone, HAZ: heat affected zone).

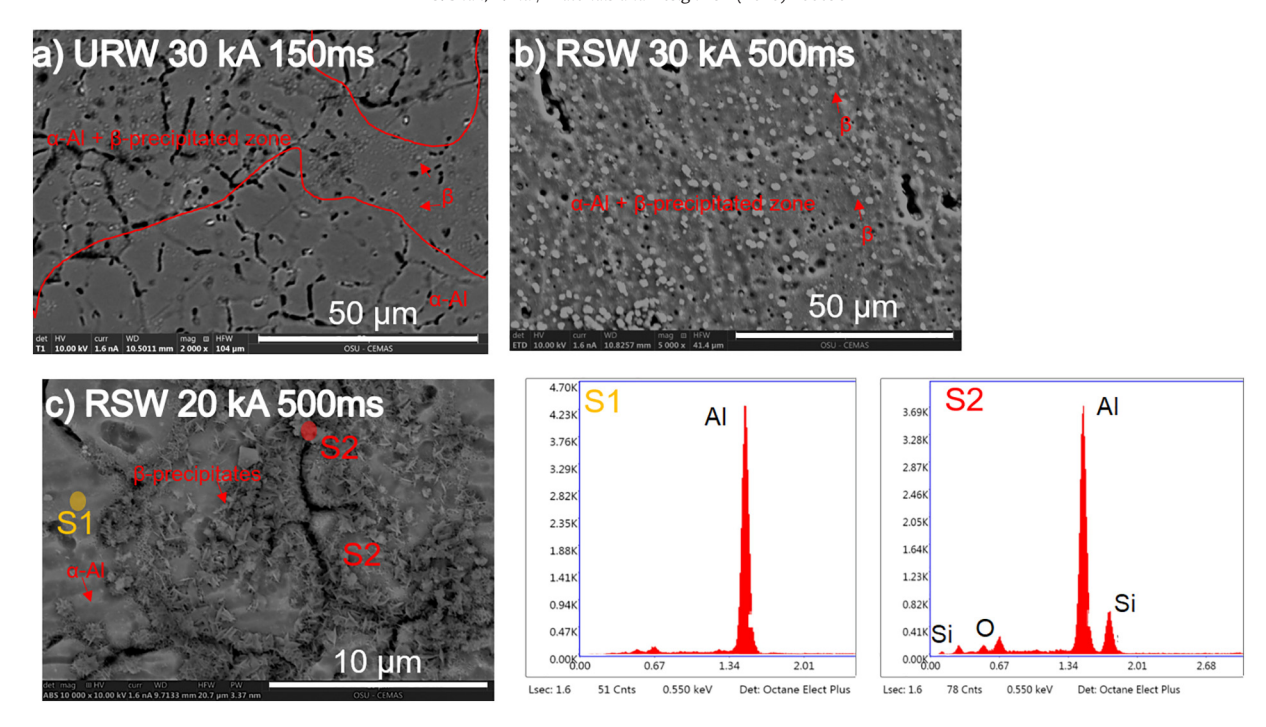


Fig. 9. SEM images of the weld microstructure at various conditions. a) center of ECZ, b) columnar zone near the center of the nugget and slight above ECZ & c) columnar zone near the center of the nugget.

URW. The actual peak temperature is not detected in this case due to the limit of the infrared camera filter.

Fig. 12 shows the top view of the temperature evolution during RSW and URW processes, which mainly provides the information at the interface between top electrode and aluminum sheet. In all the studied electrical current conditions, the peak temperature is higher in conventional RSW process than URW, which agrees with the temperature results at the interface of workpiece sheets. To further quantify the heating and cooling rates at this top contact interface to the electrode, the thermal history was extracted following the same procedure as in the side view, where the peak temperature in the area adjacent to top electrode was recorded. The results are shown in Fig. 13. Similar to the results at the interface between aluminum sheets, the electrodeworkpiece interface also shows higher heating and cooling rates in RSW than URW process.

#### 4. Ultrasonic effects on RSW process

The weld microstructure and process thermographs show that ultrasonic energy can modify the resistance spot welding process in several aspects. First is on electric contact resistance, which directly influences the formation and growth of melt nugget. The contact resistance consists of static (SECR) and dynamic electric contact resistance (DECR) [33,34]. SECR is related to the surface characteristic prior to the flow of the current, whereas DECR is a combination of interfacial resistance and bulk material resistance, which changes dynamically during the spot welding process. Both SECR and DECR directly depend on the applied electrode force, the conditions of workpiece as well as surface properties, such as elastic modulus, material flow stress, surface asperities, oxides and contaminations. It is known that ultrasonic energy can modify several of these properties [35]. Izumi et al. [36] reported 10% decrease in compressive flow stress and 30% reduction in Vickers Hardness with ultrasonic treatment of various materials. Y. Bai et al. [37] reported the surface roughness value is reduced by 42.8% via superimposed ultrasonic vibrations of 2 µm during ultrasonically assisted compression test. The increased amount of surface deformation helps fracture the oxide layer due to its limited ductility. It is known that fracture of this high resistance oxide layer can reduce the contact resistance, modifies the current density distribution and accordingly heat generation rate during RSW [38,39]. In another work carried out by E. Crinon & J. Evans [40], the effect of interfacial sliding on the electrical contact resistance of aluminum is studied. They reported a small relative rotation i.e. less than 2° could decrease the electrical contact resistance by several orders. Furthermore, in our previous study [24], the high speed video shows that in situ ultrasonic vibration facilitates breakdown of surface oxide layer and contaminants. These changes of surface conditions are reflected in the evolution of temperature field during the process, as shown in Figs. 10–13 that the peak temperature and heating rate are smaller in the URW compared with RSW process. Considering the temperature distribution and total energy input into the process, Table 2 shows that in URW process, the ultrasonic vibration adds around 2% to regular RSW process at the same electrical current condition. Despite the slightly higher energy input, the temperature is lower in the URW process. This could be explained from the aspect that main proportion of ultrasonic energy is consumed up by deforming surface asperities and breakdown of oxide layer rather than being transformed into heat.

Optical microstructure of the weld shows that the nugget size of URW is larger than RSW welds in several conditions, even though the temperature during URW process is lower. This is possibly related to the contact area and material flow in the melt pool. In situ ultrasonic vibration can soften the material during plastic deformation, known as acousto-plastic effect [41]. Under the compression force of the electrode, the surface asperities are easier to deform with the assistance of ultrasonic energy, which helps achieve a more uniform and larger contact area at the faying surface. Accordingly, this larger contact area can increase the nugget size. Besides, in the melt pool, the additional ultrasonic vibration can cause disturbance in the material flow, which homogenizes the temperature distribution and enlarges the size of the melt pool. This can also increase the nugget size without increasing maximum temperature in the weld. Further validation of these assumptions will need to be performed in future.

In the middle stage of the welding process when melting of aluminum occurs, ultrasonic energy could induce various nonlinear effects including cavitation and acoustic streaming [42]. These physical phenomena have been utilized in ultrasonic cleaning and ultrasonically

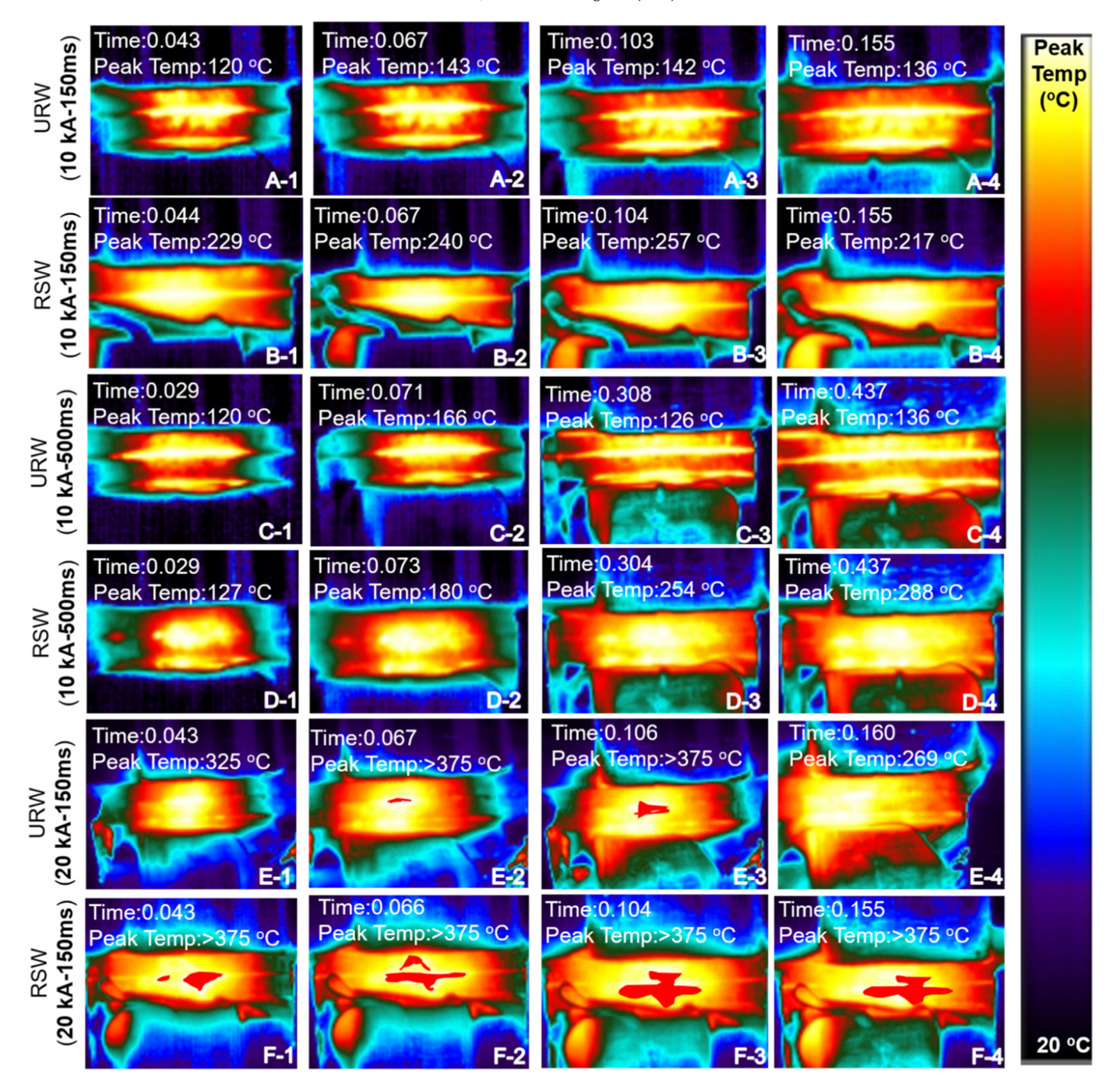


Fig. 10. Side view of the evolution of temperature distribution at various conditions. The red regions in the middle of the nugget (E2, E3, F1-F4) is due to the temperature saturation above 375 °C (maximum limit of the camera filter). (For interpretation of the references to color in this figure legend, the reader is referred to the web version of this article.)

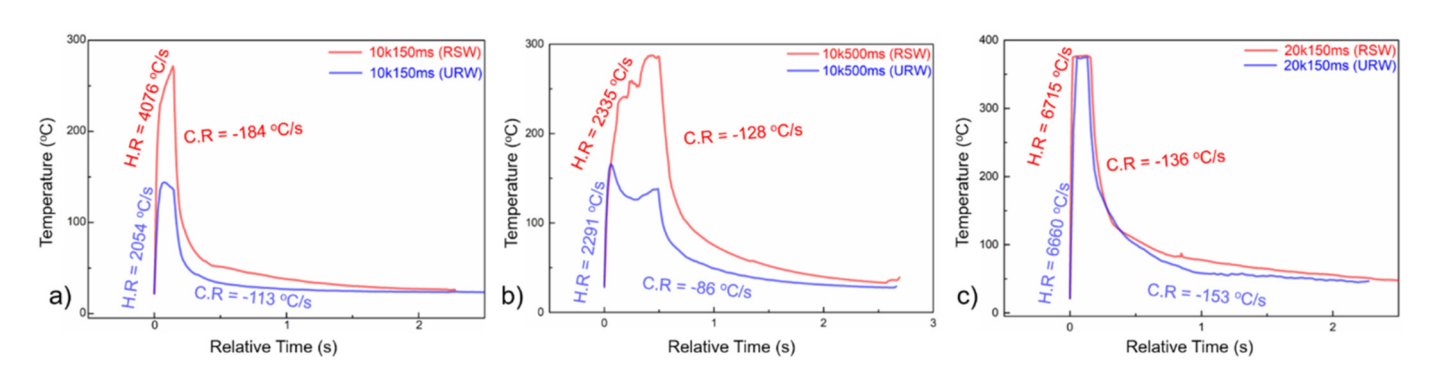
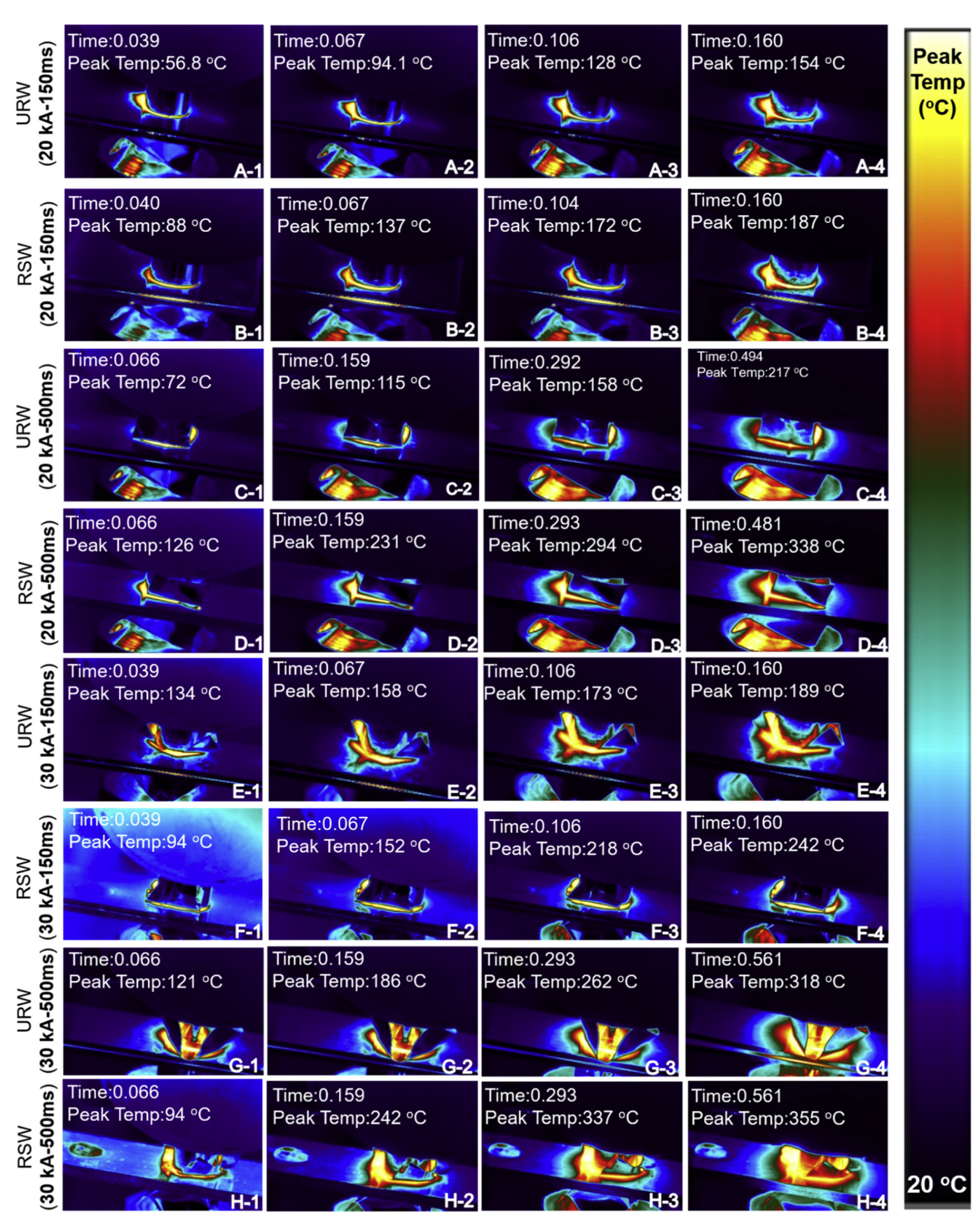


Fig. 11. Thermal history of the weld process at various conditions from the side view (Note: The thermal profile is extracted from the center of the weld nugget).



**Fig. 12.** Top view of the evolution of temperature distribution at various conditions.

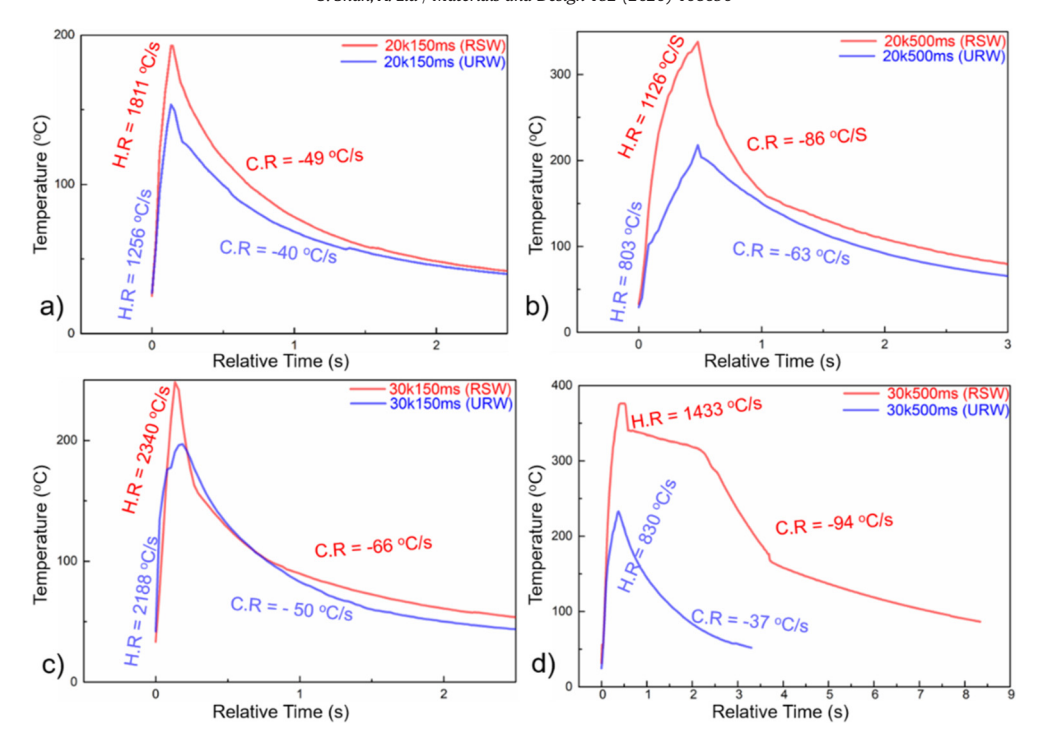


Fig. 13. Thermal history of the weld process at various conditions from the top view (Note: Thermal history is extracted from contact area between electrode and surface of the top sheet).

assisted casting process for aluminum degassing, grain refinement and elimination of casting defects such as voids and porosities [43]. Cavitation bubbles promote heterogenous nucleation during solidification, which subsequently promoted equiaxed microstructure and refines the grain size. The threshold value of ultrasonic intensity (I) to induce acoustic cavitation in aluminum melt is approximated 80 W.cm $^{-2}$  [44]. In this study, the applied ultrasonic amplitude during URW is 34  $\mu m$  (peak to peak). Accordingly, the ultrasonic intensity can be estimated based on the following equation

$$I = \frac{1}{2}\rho c \left(2\pi f A\right)^2 \tag{3}$$

where  $\rho$  is density of molten aluminum (~2375 kg.m<sup>-3</sup> at 660 °C), c is the speed of the sound in the molten aluminum (~1.3 × 10<sup>3</sup> ms<sup>-1</sup>), f is the ultrasonic frequency (19.7 kHz) and A is the vibration amplitude [44]. The estimated ultrasonic intensity in this URW process is 2734 W.cm<sup>-2</sup>, which far exceeds the threshold value to induce cavitation.

The ultrasonic vibration introduces alternating compression (high pressure) and rarefaction (low pressure) fields in the melt. Cavitation bubbles are generated in the low-pressure period, which are then collapsed during the high-pressure period and produce shock waves. The shock waves help to fracture the columnar dendrites. Acoustic streaming promotes forced convection of material and transports these dendrite fragments away to serve as additional heterogeneous nuclei. Besides, the material flow from acoustic streaming reduce macrosegregation and improve the solidification structure. This is reflected in the ECZ zone of URW welds obtained at longer duration of electrical and ultrasonic field (500 ms), which is primarily composed of single phase  $\alpha$ -Al without the bi-modal appearance. Shrinkage porosities in conventional RSW welds can also be effectively removed with the ultrasonic energy, since the potential voids can be promptly filled up by the flow of available surrounding melt from acoustic streaming.

In addition to the acoustic streaming and cavitation effect, ultrasonically reduced cooling rate (Figs. 11–13) further modifies the solidification path. All these effects contribute to the equiaxed crystal structure at

the center of the fusion nugget and a smaller columnar zone in URW welds.

#### 5. Conclusions

- URW welds of aluminum alloys show a higher mechanical strength, ductility, stiffness and energy absorbed prior to failure than RSW welds under the same electrical current condition.
- 2) Superimposed ultrasonic vibration promotes formation of equiaxed crystal zone (ECZ) in the center of the weld nugget. With short duration of electrical current and ultrasonic vibration (150 ms), ECZ comprises of a bimodal microstructure ( $\alpha$ -Al+ $\beta$ -second phase). By increasing the duration to 500 ms, the element distribution in ECZ is homogenized and results in a single phase  $\alpha$ -Al structure. For RSW welds, ECZ zone is only generated at the condition of high current and long duration, while the fusion zone consists of only columnar grain structure in the remaining conditions.
- 3) Ultrasonic vibration can effectively remove porosity defects that are observed in conventional RSW welds of aluminum alloys.
- 4) Ultrasonic vibration decreases the contact resistance and reduces the temperature distribution, heating and cooling rates.
- 5) The defect-free and refined microstructure of URW welds are achieved based on the ultrasonically induced acoustic streaming and cavitation effects, together with the modified temperature field during the process.

## **CRediT authorship contribution statement**

**Umair Shah:** Conceptualization, Methodology, Validation, Investigation, Formal analysis, Visualization, Writing - original draft. **Xun Liu:** Conceptualization, Methodology, Formal analysis, Supervision, Writing - review & editing.

## **Declaration of competing interest**

The authors declare that they have no known competing financial interests or personal relationships that could have appeared to influence the work reported in this paper.

## Acknowledgements

The project is supported by National Science Foundation under the grant No. 1853632, An Innovative Hybrid Ultrasonic Resistance Welding Process for Joining Advanced Lightweight and Dissimilar Materials. Electron microscopy was performed at the Center for Electron Microscopy and Analysis (CEMAS) at The Ohio State University. The authors would like to acknowledge T. J. Snow and Weld Computer for the resistance spot welding equipment. The authors would also like to acknowledge the valuable discussions with Dr. Avraham Benatar.

#### References

- S.M. Manladan, F. Yusof, S. Ramesh, M. Fadzil, Z. Luo, S. Ao, A review on resistance spot welding of aluminum alloys, Int. J. Adv. Manuf. Technol. 90 (2017) 605–634, https://doi.org/10.1007/s00170-016-9225-9.
- [2] Guocheng Xu, Jing Wen, C. Wang, Xiaoqi Zhang, Quality monitoring for resistance spot welding using dynamic signals, 2009 Int. Conf. Mechatronics Autom, IEEE 2009, pp. 2495–2499, https://doi.org/10.1109/ICMA.2009.5246513.
- [3] P.H. Demarois, B. Pappas, W.G. Ballard, J.R. Williams, G. West, Full scale burn test of four aluminum body ford F-150's, SAE Tech. Pap, SAE International, 2017https://doi. org/10.4271/2017-01-1355.
- [4] Z. Wan, H.-P. Wang, N. Chen, M. Wang, B.E. Carlson, Characterization of intermetallic compound at the interfaces of Al-steel resistance spot welds, J. Mater. Process. Technol. 242 (2017) 12–23, https://doi.org/10.1016/J.JMATPROTEC.2016.11.017.
- [5] P.S. James, H.W. Chandler, J.T. Evans, J. Wen, D.J. Browne, C.J. Newton, The effect of mechanical loading on the contact resistance of coated aluminium, Mater. Sci. Eng. A 230 (1997) 194–201, https://doi.org/10.1016/s0921-5093(97)00020-8.
- [6] C.J. Newton, M.C. Thornton, B.F.P. Keay, P.G. Sheasby, D.R. Boomer, How to weld bond aluminium with structural adhesives, SAE Tech. Pap, SAE International, 1997https://doi.org/10.4271/970018.
- [7] L. Han, M. Thornton, D. Boomer, M. Shergold, Effect of aluminium sheet surface conditions on feasibility and quality of resistance spot welding, J. Mater. Process. Technol. 210 (2010) 1076–1082, https://doi.org/10.1016/j.jmatprotec.2010.02.019.
- [8] Y. Zhang, H. Shan, Y. Li, C.F. Zhao, Z. Luo, J. Guo, C.Y. Ma, Effects of the oxide film on the spot joining of aluminum alloy sheets: a comparative study between resistance spot welding and resistance spot clinching, Int. J. Adv. Manuf. Technol. 92 (2017) 4231–4240, https://doi.org/10.1007/s00170-017-0387-x.
- [9] Z. Luo, S. Ao, Y.J. Chao, X. Cui, Y. Li, Y. Lin, Application of pre-heating to improve the consistency and quality in AA5052 resistance spot welding, J. Mater. Eng. Perform. 24 (2015) 3881–3891, https://doi.org/10.1007/s11665-015-1704-x.
- [10] H. Zhao, D.R. White, T. Debroy, Current issues and problems in laser welding of automotive aluminum alloys, Int. Mater. Rev. 44 (1999) 238–266, https://doi.org/10.1179/095066099101528298.
- [11] D.G. Eskin, Ultrasonic processing of molten and solidifying aluminium alloys: overview and outlook, Mater. Sci. Technol. 33 (2017) 636–645, https://doi.org/10.1080/02670836.2016.1162415.
- [12] V. Abramov, O. Abramov, V. Bulgakov, F. Sommer, Solidification of aluminium alloys under ultrasonic irradiation using water-cooled resonator, Mater. Lett. 37 (1998) 27–34, https://doi.org/10.1016/S0167-577X(98)00064-0.
- [13] G.I. Eskin, Cavitation mechanism of ultrasonic melt degassing, Ultrason. -Sonochemistry. 2 (1995) https://doi.org/10.1016/1350-4177(95)00020-7.
- [14] A. Knuutinen, K. Nogita, S.D. McDonald, A.K. Dahle, Modification of Al-Si alloys with Ba, Ca, Y and Yb, J. Light. Met. 1 (2001) 229–240, https://doi.org/10.1016/S1471-5317(02)00004-4.
- [15] S. Shivkumar, L. Wang, D. Apelian, Molten metal processing of advanced cast aluminum alloys, JOM 43 (1991) 26–32, https://doi.org/10.1007/BF03220114.
- [16] H.R. Kotadia, M. Qian, A. Das, Solidification of aluminium alloys under ultrasonication: an overview, Trans. Indian Inst. Metals 71 (2018) 2681–2686, https://doi.org/10.1007/s12666-018-1446-1.
- [17] U. Shah, X. Liu, Effects of ultrasonic vibration on resistance spot welding of transformation induced plasticity steel 780 to aluminum alloy AA6061, Mater. Des. 182 (2019), 108053. https://doi.org/10.1016/j.matdes.2019.108053.
- [18] S. Fukumoto, I. Lum, E. Biro, Y. Zhou, Welding Research-s, Weld. J. 307 (2003). https://app.aws.org/wj/supplement/11-2003-FUKUMOTO-s.pdf (accessed December 3, 2019).
- [19] W. Zhang, S.S. Ao, J.P. Oliveira, Z. Zeng, Z. Luo, Z.Z. Hao, Effect of ultrasonic spot welding on the mechanical behaviour of NiTi shape memory alloys, Smart Mater. Struct. 27 (2018) https://doi.org/10.1088/1361-665X/aacfeb.
- [20] W. Zhang, S. Ao, J.P. Oliveira, C. Li, Z. Zeng, A. Wang, Z. Luo, On the metallurgical joining mechanism during ultrasonic spot welding of NiTi using a Cu interlayer, Scr. Mater. 178 (2020) 414–417, https://doi.org/10.1016/j.scriptamat.2019.12.012.

- [21] S.M.A.K. Mohammed, S.S. Dash, X.Q. Jiang, D.Y. Li, D.L. Chen, Ultrasonic spot welding of 5182 aluminum alloy: evolution of microstructure and mechanical properties, Mater. Sci. Eng. A 756 (2019) 417–429. https://doi.org/10.1016/j.msea.2019.04.059.
- [22] J. Yang, B. Cao, Investigation of resistance heat assisted ultrasonic welding of 6061 aluminum alloys to pure copper, Mater. Des. 74 (2015) 19–24, https://doi.org/10. 1016/j.matdes.2015.02.028.
- [23] U.H. Shah, X. Liu, Ultrasonic resistance welding of TRIP-780 steel, J. Mater. Process. Technol. 274 (2019) https://doi.org/10.1016/j.jmatprotec.2019.116287.
- [24] U. Shah, X. Liu, Effects of ultrasonic vibration on resistance spot welding of transformation induced plasticity steel 780 to aluminum alloy AA6061, Mater. Des. 182 (2019) https://doi.org/10.1016/j.matdes.2019.108053.
- [25] A. S, A.M.P. de Jesus, Fatigue behaviour of welded joints made of 6061-T651 aluminium alloy, Alum. Alloy. Theory Appl, InTech, 2011https://doi.org/10.5772/14489.
- [26] Y. Sun, N. Tsuji, H. Fujii, Microstructure and mechanical properties of dissimilar friction stir welding between ultrafine grained 1050 and 6061-T6 aluminum alloys, Metals (Basel) 6 (2016) 249, https://doi.org/10.3390/met6100249.
- [27] M.I. Khan, M.L. Kuntz, Y. Zhou, Effects of weld microstructure on static and impact performance of resistance spot welded joints in advanced high strength steels, Sci. Technol. Weld. Join. 13 (2008) 294–304, https://doi.org/10.1179/ 174329308X771733
- [28] M. Pouranvari, H.R. Asgari, S.M. Mosavizadch, P.H. Marashi, M. Goodarzi, Effect of weld nugget size on overload failure mode of resistance spot welds, Sci. Technol. Weld. Join. 12 (2007) 217–225, https://doi.org/10.1179/174329307X164409.
- [29] M. Pouranvari, S.P.H. Marashi, Failure of resistance spot welds: tensile shear versus coach peel loading conditions, Ironmak. Steelmak. 39 (2012) 104–111, https://doi. org/10.1179/1743281211Y.000000066.
- [30] Y. Li, F. Yan, Z. Luo, Y.J. Chao, S. Ao, X. Cui, Weld growth mechanisms and failure behavior of three-sheet resistance spot welds made of 5052 aluminum alloy, J. Mater. Eng. Perform. 24 (2015) 2546–2555, https://doi.org/10.1007/s11665-015-1519-9.
- [31] A.M. Pereira, J.M. Ferreira, A. Loureiro, J.D.M. Costa, P.J. Bártolo, Effect of process parameters on the strength of resistance spot welds in 6082-T6 aluminium alloy, Mater. Des. 31 (2010) 2454–2463, https://doi.org/10.1016/j.matdes.2009.11.052.
- [32] Y. Li, Z. Luo, F. Yan, R. Duan, Q. Yao, Effect of external magnetic field on resistance spot welds of aluminum alloy, Mater. Des. 56 (2014) 1025–1033, https://doi.org/ 10.1016/j.mardes.2013.12.005.
- [33] W.F. Savage, E.F. Nippes, F.A. Wassell, Dynamic Contact Resistance of Series Spot Welds some Effects of Electrode Force, Current, and Material Surface Condition on the Dynamic Resistance of Spot Welds Are Determined for Different Uncoated and Galvanized Auto-Body Steel Combinations, n.d..
- [34] W.F. Savage, E.F. Nippes, F.A. Wassell, Static Contact Resistance of Series Spot Welds Studies Are Conducted on the Effects of Electrode Force, Current, and Surface Conditions on Static Contact Resistance before and after Spot Welding of Uncoated and Galvanized Auto-Body Steel, n.d..
- [35] A. Siddiq, T. El Sayed, Ultrasonic-assisted manufacturing processes: variational model and numerical simulations, Ultrasonics 52 (2012) 521–529, https://doi.org/ 10.1016/j.ultras.2011.11.004.
- [36] O. Izumi, K. Oyama, Y. Suzuki, Effects of superimposed ultrasonic vibration on compressive deformation of metals, Trans. Japan Inst. Met. 7 (1966) 162–167, https://doi.org/10.2320/matertrans1960.7.162.
- [37] Y. Bai, M. Yang, The influence of superimposed ultrasonic vibration on surface asperities deformation, J. Mater. Process. Technol. 229 (2016) 367–374, https://doi.org/10.1016/j.jmatprotec.2015.06.006.
- [38] C. Ruirun, Z. Deshuang, M. Tengfei, D. Hongsheng, S. Yanqing, G. Jingjie, F. Hengzhi, Effects of ultrasonic vibration on the microstructure and mechanical properties of high alloying TiAl, Sci. Rep. 7 (2017) https://doi.org/10.1038/srep41463.
- [39] E.P. Patrick, J.R. Auhl, T.S. Sun, Understanding the process mechanisms is key to reliable resistance spot welding aluminum auto body components, SAE Trans. 93 (1984) 435–448, https://doi.org/10.2307/44434260.
- [40] E. Crinon, J.T. Evans, The effect of surface roughness, oxide film thickness and interfacial sliding on the electrical contact resistance of aluminium, Mater. Sci. Eng. A 242 (1998) 121–128, https://doi.org/10.1016/s0921-5093(97)00508-x.
- [41] A. Deshpande, K. Hsu, Acoustic energy enabled dynamic recovery in aluminium and its effects on stress evolution and post-deformation microstructure, Mater. Sci. Eng. A (2018) https://doi.org/10.1016/j.msea.2017.11.015.
- [42] D.G. Eskin, I. Tzanakis, F. Wang, G.S.B. Lebon, T. Subroto, K. Pericleous, J. Mi, Fundamental studies of ultrasonic melt processing, Ultrason. Sonochem. 52 (2019) 455–467, https://doi.org/10.1016/j.ultsonch.2018.12.028.
- [43] G.I. Eskin, Ultrasonic Treatment of Light Alloy Melts, CRC Press, 2017.
- [44] G. Wang, Q. Wang, M.A. Easton, M.S. Dargusch, M. Qian, D.G. Eskin, D.H. StJohn, Role of ultrasonic treatment, inoculation and solute in the grain refinement of commercial purity aluminium, Sci. Rep. 7 (2017) https://doi.org/10.1038/s41598-017-10354-6.